Article

Discovery Medicine 2026; 38(205): 574–586
https://doi.org/10.24976/Discov.Med.202638205.47

Oxaliplatin Combined With a PD-1 Inhibitor Synergistically Suppresses Gastric Cancer Growth via STEAP4-Mediated Ferroptosis

Yuxiu Zou[1,2,†], Fengxue Dai[3,†], Li Feng[4,*], Xiaoqiong Jia[3,*]

[1]Inner Mongolia Medical University, 010110 Hohhot, Inner Mongolia Autonomous Region, China
[2]Department of Integrated Traditional Chinese and Western Medicine for Cancer Palliative Care, Peking University Cancer Hospital Inner Mongolia Hospital, Affiliated Tumor Hospital of Inner Mongolia Medical University, 010020 Hohhot, Inner Mongolia Autonomous Region, China
[3]Department of Day Oncology Unit, Peking University Cancer Hospital Inner Mongolia Hospital, Affiliated Tumor Hospital of Inner Mongolia Medical University, 010020 Hohhot, Inner Mongolia Autonomous Region, China
[4]Surgical Oncology of Gastrointestinal Tract, Peking University Cancer Hospital Inner Mongolia Hospital, Affiliated Tumor Hospital of Inner Mongolia Medical University, 010020 Hohhot, Inner Mongolia Autonomous Region, China
*Correspondence: feng_zhuo1@126.com (Li Feng); jiaxiaoqiong2005@126.com (Xiaoqiong Jia)
[†]These authors contributed equally.
Submitted: 29 October 2025 Revised: 22 December 2025 Accepted: 31 December 2025 Published: 20 February 2026

Background: Gastric cancer (GC) has a poor response to current chemo-immunotherapy. Ferroptosis is a newly recognised form of iron-dependent cell death that can enhance drug efficacy; however, the key regulator factors and mechanisms governing ferroptosis in gastric cancer remain unclear. This study aimed to investigate the synergistic antitumor effect of oxaliplatin combined with a programmed death-1 (PD-1) inhibitor in gastric cancer and elucidate the regulatory role of six-transmembrane epithelial antigen of prostate 4 (*STEAP4*) in ferroptosis.

Methods: Subcutaneous mouse forestomach carcinoma (MFC) gastric cancer xenograft models were successfully developed using immunodeficient BALB/c nude mice and randomized into control, oxaliplatin, PD-1 inhibitor, and combination groups for *in vivo* efficacy assessment. *In vitro*, *STEAP4* was silenced in MFC cells via siRNA to evaluate its impact on drug sensitivity. Western blotting, qRT-PCR (Quantitative Reverse Transcription Polymerase Chain Reaction), transmission electron microscopy, and biochemical assays were used to detect *STEAP4* expression and ferroptosis-related markers.

Results: The combination treatment significantly suppressed tumor growth compared with monotherapies ($p < 0.01$). Mechanistically, it induced ferroptosis, characterized by mitochondrial shrinkage, increased Fe^{2+} and ROS (Reactive Oxygen Species) levels, upregulation of ACSL4, and downregulation of glutathione peroxidase 4 (GPX4) and SLC7A11. *STEAP4* expression was markedly elevated in tumor tissues after combination therapy ($p < 0.01$). *STEAP4* knockdown reduced the sensitivity of MFC cells to the combination and reversed ferroptosis induction by suppressing ACSL4 and restoring GPX4 and SLC7A11 expression.

Conclusion: The combination of oxaliplatin and a PD-1 inhibitor exerts potent synergistic effects in gastric cancer through *STEAP4* upregulation, which promotes ferroptosis and enhances treatment sensitivity. *STEAP4* may serve as a potential biomarker and therapeutic target for optimizing combination therapy in gastric cancer.

Keywords: gastric cancer; oxaliplatin; PD-1 inhibitor; *STEAP4*; ferroptosis; combination therapy

Introduction

Gastric cancer (GC) is the third deadliest malignancy worldwide, with half of cases and deaths occurring in East Asia [1]. This high burden is closely linked to specific environmental and genetic factors in the region [2]. Owing to the absence of characteristic early symptoms, most patients are diagnosed at advanced stages, losing the opportunity for curative resection and facing poor prognosis [3]. Systemic chemotherapy based on platinum and fluoropyrimidines remains a standard treatment for advanced GC. Oxaliplatin, a third-generation platinum compound, is widely used due to its favorable efficacy and manageable toxicity. Oxaliplatin-based regimens (e.g., FOLFOX) achieve superior objective response and progression-free survival compared with cisplatin, accompanied by lower neurotoxicity and nephrotoxicity in advanced GC [4,5]. Nevertheless, the objective response to chemotherapy remains limited, and the inevitable emergence of drug resistance is a major barrier to durable clinical efficacy.

Immune checkpoint inhibitors (ICIs) directed against programmed death-1 (PD-1) and its ligand (PD-L1) have redefined treatment landscapes for multiple solid tumours by reactivating exhausted cytotoxic T cells and restoring antitumour immune surveillance [6,7]. Inhibition of the PD-1/PD-L1 axis reverses tumor-induced T cell exhaustion and

reactivates immune surveillance [8,9]. Although PD-1 inhibitors have demonstrated durable responses in a subset of patients with advanced GC, the overall objective response rate to monotherapy remains suboptimal, benefiting only 10–20% of patients [10,11]. Therefore, developing combination strategies that enhance the efficacy of ICIs and broaden the patient population that benefits from them is urgently needed.

Chemotherapy–immunotherapy combinations are considered a promising approach. Chemotherapeutic agents can trigger immunogenic cell death (ICD), leading to tumor-specific antigens and damage-associated molecular patterns (DAMPs) increasing tumor immunogenicity. Additionally, chemotherapy can remodel the tumor microenvironment by depleting immunosuppressive cells and enhancing infiltration and activity of effector T cells [12–14]. This synergistic interaction provides a mechanistic basis for overcoming resistance to immunotherapy.

Ferroptosis is a recently identified form of regulated cell death dependent on iron, characterized by distinct morphological and biochemical features compared with apoptosis and necrosis. Its central mechanism involves inactivation of glutathione peroxidase 4 (GPX4), leading to uncontrolled lipid peroxide accumulation [15,16]. Increasing evidence indicates that ferroptosis induction is an effective anticancer strategy, and that chemotherapy, radiotherapy, and immunotherapy may exert part of their effects through ferroptotic pathways [17,18].

Six-transmembrane epithelial antigen of prostate 4 (*STEAP4*), also known as metalloreductase, participates in intracellular copper and iron metabolism and maintains redox homeostasis [19,20]. Aberrant expression of *STEAP4* has been reported in various tumors and is associated with tumor proliferation, invasion, and metabolic reprogramming [21]. Given its role in metal ion metabolism, *STEAP4* could potentially regulate ferroptosis. However, its specific biological function in GC and its potential role in modulating the antitumor effects of oxaliplatin combined with PD-1 inhibitors remain undefined.

Therefore, we developed *in vivo* and *in vitro* GC models to evaluate the synergistic antitumor effects of oxaliplatin in this combination therapy through ferroptosis induction. It also clarified the contribution of *STEAP4* to this process, aiming to elucidate the underlying mechanisms and identify potential therapeutic targets for combination strategies in GC.

Materials and Methods

Cell Culture

The murine gastric cancer cell line MFC (Cat. #C5106) was obtained from Zhejiang Baidi Biotechnology Co., Ltd. (BDBIO, China). Upon receipt, the cells were expanded for two passages, then authenticated by short-tandem-repeat (STR) profiling (BDBIO, China), and confirmed to be 96% identical to the reference MFC profile. A frozen master stock was prepared immediately after authentication. All experiments were performed within 10 passages from this stock. Cells are tested for mycoplasma contamination; only mycoplasma-negative cultures were used. MFC cells were cultured in DMEM high-glucose medium (Cat. #11965175, Gibco, USA) supplemented with 10% fetal bovine serum (FBS, Cat. #26140079, Gibco, USA) and 1% penicillin–streptomycin (Cat. #15140122, Gibco, USA) at 37 °C in a humidified incubator with 5% CO_2. Cells were passaged using 0.25% trypsin (Cat. #25200072, Gibco, USA).

Cell siRNA Transfection

For siRNA transfection, cells were seeded into six-well plates at an appropriate density. siRNA targeting *STEAP4* (sense: 5′-GGUGUUUGUCUGUGGAAAUGA-3′, antisense: 5′-AUUUCCACAGACAAACACCUG-3′) and negative control siRNA (si-NC: sense: 5′-UUCUCCGAACGUGUCACGUTT-3′, antisense: 5′-ACGUGACACGUUCGGAGAATT-3′) were designed and synthesized using GenePharma (Shanghai, China). When cell confluence reached 50–60%, 50 nM si-*STEAP4* or si-NC was diluted in serum-free medium and mixed with Lipofectamine™ 3000 reagent (Cat. #L3000015, Invitrogen, USA) according to the manufacturer's instructions. Following a 15-min incubation period at room temperature, the mixture solution was administered to the wells using a dropwise method. Upon completion of the 6-hour transfection period, the culture medium was exchanged with fresh complete medium, and cells were cultured for an additional 24–48 h before further assays.

Animal Model and Treatment

Male BALB/c nude mice (4–6 weeks old, 18–22 g; Beijing Vital River Laboratory Animal Technology Co., Ltd., China) were acclimatized for one week under specific pathogen-free (SPF) conditions. MFC cells in logarithmic growth phase were resuspended in sterile PBS (Beijing, China) at 5×10^7 cells/mL. Each mouse was injected subcutaneously in the right axilla with 100 µL of MFC cell suspension (5×10^6 cells). Once the average tumor volume approached approximately 100 mm^3, mice were allocated into experimental groups (n = 6/group): (i) model control (intraperitoneal injection of 0.9% saline, 10 mL/kg, twice weekly (Monday & Thursday) for 3 consecutive weeks), (ii) oxaliplatin group (5 mg/kg, dissolved in 5% glucose, 0.2 µm-filtered), (iii) PD-1 inhibitor group (anti-PD-1 antibody, 10 mg/kg, reconstituted in sterile PBS, 1 mg/mL stock), or (iv) combination group (oxaliplatin (5 mg/kg) + anti-PD-1 (10 mg /kg) prepared in separate syringes and injected consecutively on the same day, same volume and frequency as above). Oxaliplatin (purity ≥99%; Cat# S1224, Selleck Chemicals, Houston, TX, USA) was dissolved in 5% glucose and stored at –80 °C. Anti-mouse PD-1 anti-

body (clone RMP1-14; Cat# BE0146, BioXCell, Lebanon, NH, USA) was stored at 4 °C and used within 4 weeks of reconstitution. Drugs were administered intraperitoneally twice weekly for three weeks. Mice were randomly assigned to groups (n = 6 per group). Two animals in each group that did not meet the pre-established inclusion criteria were excluded; consequently, data from four biologically independent mice per group were used for statistical analysis. All the animal experiments complied with the guidelines of the Tianjin Medical Experimental Animal Care, and animal protocols were approved by the Institutional Animal Care and Use Committee of Yi Shengyuan Gene Technology (Tianjin) Co., Ltd. (protocol number YSY-DWLL-2023809).

Tumor Growth Monitoring and Histological Assessment

From the first day of treatment, tumor length (L) and width (W) were measured weekly using a digital caliper, and tumor volume (V) was calculated as $V = 0.5 \times L \times W^2$. Tumor growth curves were plotted. Upon completion of treatment, mice were euthanized by cervical dislocation, followed by tumor excision, weight measurement, and photographic documentation. Portions of tumor tissue were fixed in 4% paraformaldehyde for histological examination, and the remaining samples were snap-frozen with liquid nitrogen and maintained at –80 °C for long-term storage.

Intracellular Reactive Oxygen Species (ROS) Assays

Intracellular ROS levels were measured with the commercial Reactive Oxygen Species Assay Kit (Cat#CA1410, Solarbio, Beijing, China). MFC cells were trypsinized, resuspended at 1×10^6 cells mL^{-1} in RPMI-1640 containing 10 μM DCFH-DA fluorescent probe (Cat# S0034S, Beyotime) (1:1000 dilution of the supplied 10 mM stock) and incubated for 30 min at 37 °C, 5% CO_2 in the dark, with gentle mixing every 5 min. After three washes in serum-free medium, fluorescence (488 nm) was acquired immediately by flow cytometry with BD FACSCaliburTM Flow Cytometer (Cat# E97501093, BD Biosciences, USA).

Western Blotting

Frozen tumor or cell samples were lysed in RIPA buffer (Cat# P0013B, Beyotime Biotechnology, Shanghai, China) containing protease and phosphatase inhibitors on ice for 30 min. Lysates were centrifuged at 12,000 rpm at 4 °C for 15 min, and protein concentration was determined using BCA protein assay kit (Cat# P0012, Beyotime Biotechnology, Shanghai, China). Equal amounts of protein (30 μg/lane) were separated by 10% SDS-PAGE and transferred to PVDF (Polyvinylidene Fluoride) membranes (Cat# FFP20, Beyotime Biotechnology, Shanghai, China). Membranes were blocked with 5% nonfat milk in TBST for 1.5 h at room temperature, incubated overnight at 4 °C with primary antibodies: ACSL4 (Cat# 22401-1-AP, 150UL, Proteintech, Wuhan, China, 1:1000), DMT1 (Cat# 20507-1-AP, Proteintech, Wuhan, China, 1:1000), GPX4 (Cat# 67763-1-Ig, Proteintech, Wuhan, China, 1:1000), HSBP1 (Cat# 10169-2-AP, Proteintech, Wuhan, China, 1:1000), SLC7A11 (Cat# 98051, CST, MA, USA, 1:1000), *STEAP4* (Cat# 68465-1-Ig, Proteintech, Wuhan, China, 1:1000); β-actin (Cat# 66009-1-Ig, Proteintech, Wuhan, China, 1:5000), then washed, and incubated with secondary antibody: HRP-conjugated Goat Anti-Mouse IgG (H+L) (Cat# SA00001-1, Proteintech, Wuhan, China, 1:5000) or HRP-conjugated Goat Anti-Rabbit IgG (H+L) (Cat# SA00001-2, Proteintech, Wuhan, China, 1:5000) for 1 h at room temperature. Protein bands were visualized using ECL chemiluminescence kit (Cat# P0018FS, Beyotime Biotechnology, Shanghai, China) and imaged with an Image Lab system (Bio-Rad ChemiDoc, California, USA). Band intensities were quantified using ImageJ software (v1.53, National Institutes of Health (NIH), Baltimore, MD, USA) and normalized to the internal control.

Quantitative Real-Time PCR (qRT-PCR)

The isolation of total RNA from cells or tissues was performed utilizing TRIzol reagent (Cat# TR-01, Foregene, China). Subsequently, RNA quantification and assessment of purity were conducted by measuring absorbance at 260 nm and 280 nm wavelengths with a NanoDrop 2000 (Cat# 13-400-504, Thermo Fisher Scientific, USA). A quantity of 1 μg total RNA was converted to complementary DNA using a commercial reverse transcription system (Cat. No: QP056, GeneCopeia, Rockville, MD, USA) according to the manufacturer's protocol. qRT-PCR was performed with SYBR Green Master Mix (Cat# G3320, Servicebio, Wuhan, China) on a real-time PCR system (CFX Maestro,v4.1.2433.1219, Bio-Rad, USA). Cycling conditions were as follows: 95 °C for 30 s, followed by 40 amplification cycles of 95 °C for 5 s and extension 60 °C for 30 s. GAPDH served as the endogenous reference gene, and quantitative analysis of gene expression levels was performed utilizing the $2^{-\Delta\Delta Ct}$ method. The primer sequences used were as follows:

STEAP4 forward, 5′-AGAGTCAAATGCGGAATA-3′, and reverse, 5′-GAAATAGTTGCAGAGGGTAG-3′;

SLC7A11 forward, 5′-AATACGGAGCCTTCCACG AG-3′, and reverse, 5′-ACTGTTCGGTCGTGACTTCC-3′;

GPX4 forward, 5′-GCCGTCTGAGCCGCTTACTT-3′, and reverse, 5′-TATCGGGCATGCAGATCGAC-3′;

ACSL4 forward, 5′-CCTTCCTCTTAAGGCCGGGA -3′, and reverse, 5′-TCTTTGCCATAGCGTTTTTCTTAG-3′;

HSBP1 forward, 5′-ATGAGTGGTCGCAGTGGTT C-3′, and reverse, 5′-TTCGTGCTTGCCAGTGATCT-3′;

DMT1 forward, 5′-GTTCTCCAACGGAATAGGC-3′, and reverse, 5′-CCAACGCAATCAAACACT-3′;

GAPDH forward, 5′-ATCACGCCACAGCTTTCCAG-3′, and reverse, 5′-GCCAGTAGAGGCAGGGATGATGTTC-3′.

Fe^{2+} and NADPH (Nicotinamide Adenine Dinucleotide Phosphate) Measurement

The concentration of ferrous ions (Fe^{2+}) was quantified employing a colorimetric ferrous ion assay kit (Cat# E-BC-K881-M, Elabscience, China). Simultaneously, NADPH levels were assessed using a standardized $NADP^+$/NADPH quantification kit (Cat# S0179, Beyotime, Shanghai, China). Assays were performed according to the manufacturers' protocols, and absorbance measurement was conducted with a Bio-Rad iMark microplate reader (168-1130, Model iMark, Bio-Rad, USA).

Transmission Electron Microscopy (TEM)

Tumor tissues were fixed in 2.5% glutaraldehyde (Cat# 111-30-8, Sigma-Aldrich, USA) at 4 °C for 12 hours. Following this, the samples were washed three times with PBS, post-fixed in 1% osmium tetroxide (Cat# 419494, Sigma-Aldrich, USA) for 2 h, dehydrated in graded acetone, and embedded in Epon 812 resin for further processing. Ultrathin sections (70 nm) were stained with uranyl acetate and lead citrate solution, and mitochondrial ultrastructure was examined with a Hitachi HT7700 TEM microscope (HITACHI, Japan).

Histopathology

Sections (5 µm) were subjected to hematoxylin–eosin (HE) staining to evaluate morphology and inflammatory cell infiltration. Apoptosis was assessed using a TUNEL (TdT-mediated dUTP Nick-End Labeling) assay kit (Cat# G1504, Servicebio, Wuhan, China) with DAPI nuclear counterstaining. PCNA expression was analyzed by immunofluorescence after deparaffinization, rehydration, antigen retrieval, blocking, and incubation with primary antibody (anti-PCNA: Cat# GB11010, Servicebio, Wuhan, China, 1:500) at 4 °C overnight, followed by a fluorochrome-conjugated secondary antibody (FITC-labeled Goat Anti-Rabbit IgG (H+L), Cat# GB22303, Servicebio, Wuhan, China, 1:200) for 2 h at room temperature. Images were captured under a fluorescence microscope (Nikon Instruments Inc., Tokyo, Japan), and mean fluorescence intensity was quantified using ImageJ (v1.53, National Institutes of Health, Bethesda, MD, USA).

Transcriptome Sequencing and Bioinformatics Analysis

RNA-seq was performed on human gastric cancer and adjacent noncancerous tissues using the Illumina NovaSeq 6000 platform. After quality control and adapter trimming, reads were aligned to the human reference genome. Differentially expressed genes (fold change >1.5, adjusted p-value < 0.05) were identified using DESeq2. Ferroptosis-related genes were obtained from public databases and intersected with differentially expressed genes. Volcano plots, Venn diagrams, KEGG pathway enrichment, and GO analysis were generated, and heatmaps were plotted.

Cellular Functional Assays

Cell viability was assessed using the CCK-8 (Cell Counting Kit-8) assay. MFC cells (5×10^3/well) were seeded into 96-well plates, treated with the indicated drugs or siRNA for 48 h, and incubated with 10 µL CCK-8 reagent (Cat# C0037, Beyotime Biotechnology, Shanghai, China) for 2 h at 37 °C. Optical density (OD) was measured at 450 nm using a microplate reader.

Cell apoptosis was assessed using Flow cytometry. MFC cells (5×10^3/well) were harvested without trypsin (EDTA-free cell scraper), washed twice with ice-cold PBS, and resuspended in 1× Annexin V binding buffer (Cat#556454, BD Biosciences, USA). Five microlitres of FITC-conjugated Annexin V (Cat#556419, BD Biosciences) and 5 µL of propidium iodide (PI, 50 µg mL^{-1}, Cat#556463, BD Biosciences) were added, and cells were incubated for 15 min at 25 °C in the dark. Samples were analysed within 1 h on a BD Accuri C6 Plus flow cytometer (BD Biosciences, San Jose, CA, USA) equipped with a 488 nm laser. Data were processed with FlowJo (v10.8.1; FlowJo LLC, Ashland, OR, USA); early apoptotic (Annexin V^+/PI^-) and late apoptotic/necrotic (Annexin V^+/PI^+) populations were summed and reported as total apoptosis percentage.

Cell migration and invasion were assessed using Transwell assay. For migration, cells in 200 µL serum-free medium were seeded into the upper chamber of Transwell inserts (8 µm pores, Cat#3422, Corning, USA). For invasion, the upper surface was pre-coated with Matrigel (Cat#356234, 1:8, Corning, USA). Complete medium with 10% FBS (600 µL) served as chemoattractant. After 24 h (migration) or 36 h (invasion), cells on the lower surface were fixed with 4% paraformaldehyde, stained with 0.1% crystal violet (Cat#C3886, Sigma-aldrich, USA), and counted in five random fields per filter (×200 magnification).

Statistical Analysis

All experiments were performed independently at least three times. Data were analyzed and visualized using GraphPad Prism software (version 8.0, GraphPad Software, LLC, San Diego, CA, USA). Results are expressed as mean ± standard deviation (SD). Comparisons between two groups were performed using an unpaired Student's t-test, and multiple group comparisons were conducted using one-way ANOVA with subsequent Tukey's multiple comparison tests. A p-value < 0.05 was deemed statistically significant.

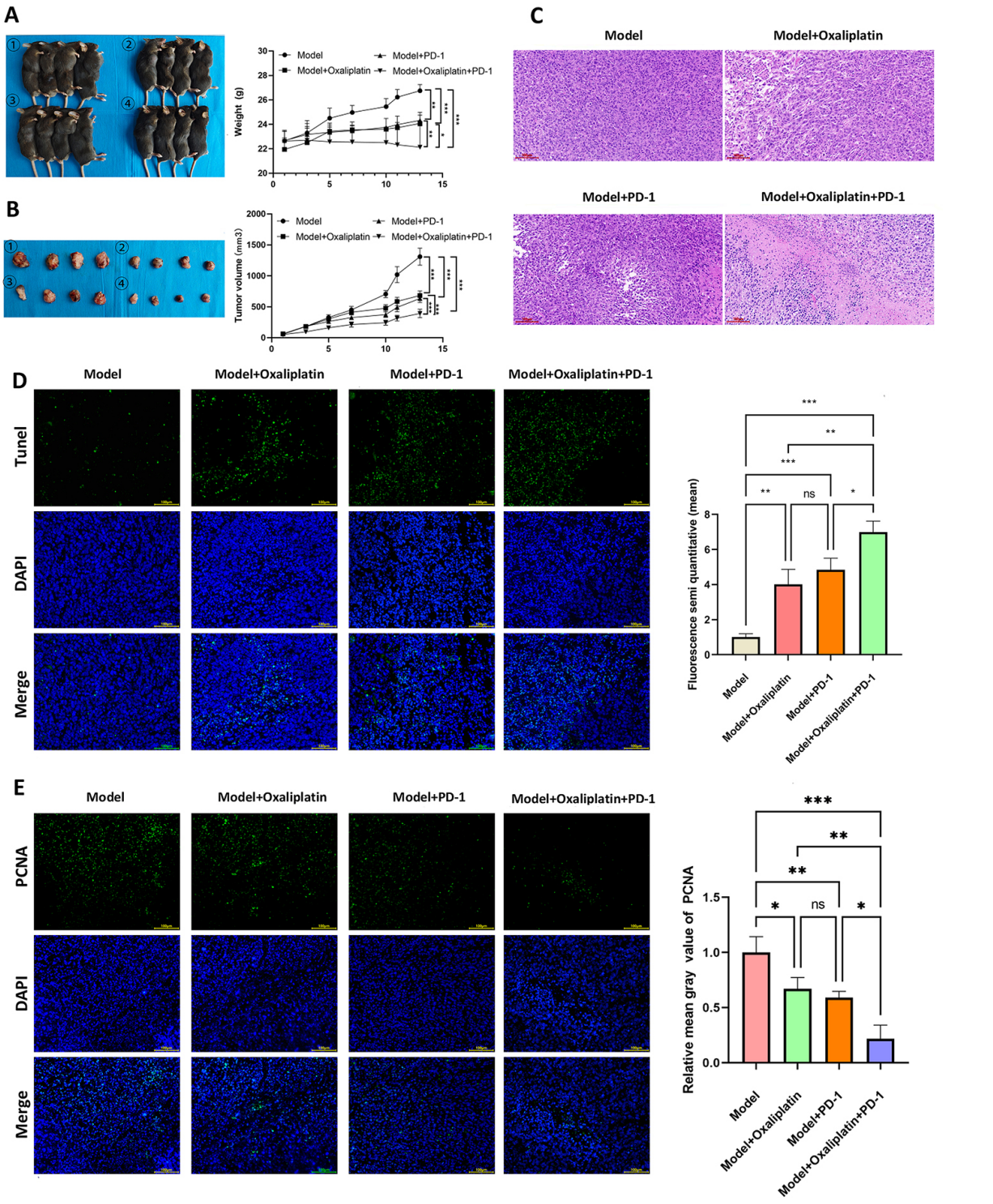

Fig. 1. Oxaliplatin combined with a PD-1 inhibitor synergistically suppresses gastric tumor growth *in vivo*. (A) Representative gross images of subcutaneous xenograft tumors in each group after treatment (n = 4). The numbers 1, 2, 3, and 4 indicate the Model, Oxaliplatin, PD-1 inhibitor, and Combination treatment groups, respectively. (B) Tumor weight statistics for each group (n = 4). The numbers 1, 2, 3, and 4 indicate the Model, Oxaliplatin, PD-1 inhibitor, and Combination treatment groups, respectively. (C) Hematoxylin–eosin (H&E) staining of tumor tissues (scale bar = 100 μm). (D) TUNEL staining of tumor tissues showing apoptotic cells (green) and nuclei (blue) (scale bar = 100 μm). (E) Immunofluorescence staining of the proliferation marker PCNA in tumor tissues (green: PCNA-positive cells; blue: nuclei) (scale bar = 100 μm). Data in (D) and (E) are presented as mean ± SD from three biologically independent experiments. ns: not significant, *$p < 0.05$, **$p < 0.01$, ***$p < 0.001$.

Results

Oxaliplatin Combined With a PD-1 Inhibitor Synergistically Suppresses the Growth of Gastric Cancer Xenografts In Vivo

To evaluate the *in vivo* antitumor efficacy of oxaliplatin in combination with a PD-1 inhibitor, we established a subcutaneous xenograft model using MFC gastric cancer cells. At the end of the treatment period, significant differences in tumor size were observed among the groups (Fig. 1A,B). Compared with the model group, treatment with either oxaliplatin or the PD-1 inhibitor alone significantly inhibited tumor growth ($p < 0.01$); however, the combination therapy achieved the most pronounced effect, with both tumor volume and weight substantially reduced compared to all other groups ($p < 0.01$). In contrast, no significant differences were detected between the two monotherapy groups.

Histological analysis with H&E staining revealed that tumors from the combination group exhibited a markedly reduced cell density and expanded necrotic areas, indicating more pronounced growth suppression (Fig. 1C). TUNEL staining further showed that, while treatment with either oxaliplatin or the PD-1 inhibitor alone significantly induced apoptosis ($p < 0.01$), the combination treatment yielded the strongest apoptotic response ($p < 0.001$) (Fig. 1D). Immunofluorescence staining for PCNA demonstrated that both monotherapies reduced PCNA expression ($p < 0.05$), whereas the combination therapy resulted in the most substantial suppression ($p < 0.001$) (Fig. 1E). Collectively, these findings indicate that oxaliplatin and a PD-1 inhibitor, together, exert a strong synergistic antitumor effect against gastric cancer *in vivo*.

Oxaliplatin Combined With a PD-1 Inhibitor Exerts Antitumor Effects by Inducing Ferroptosis

To determine whether the synergistic antitumor effect of oxaliplatin combined with the PD-1 inhibitor involved ferroptosis, multiple ferroptosis-related parameters were examined in tumor tissues from treated mice. Transmission electron microscopy revealed intact mitochondrial morphology with well-defined cristae in the model group, while mitochondria in tumors from either monotherapy group exhibited varying degrees of structural damage. Notably, tumors from the combination group displayed characteristic ultrastructural alterations consistent with ferroptosis, manifested by diminished mitochondrial size, elevated membrane electron density, and partial or complete loss of cristae structures, strongly suggesting ferroptotic cell death (Fig. 2A).

Given that ferroptosis is dependent on iron accumulation, we quantified Fe^{2+} levels in tumor tissues. Compared with the model group, Fe^{2+} concentration increased slightly in the two monotherapy groups ($p < 0.05$), whereas the combination treatment resulted in an elevation in Fe^{2+} levels ($p < 0.001$), indicating enhanced intracellular iron accumulation conducive to ferroptosis (Fig. 2B). NADPH depletion, which compromises the cellular antioxidant defense system, is closely associated with ferroptosis. The combination treatment resulted in a marked reduction in NADPH levels compared to the model ($p < 0.001$) and monotherapy groups ($p < 0.01$), suggesting that combination therapy promotes ferroptosis by depleting NADPH and disrupting redox homeostasis (Fig. 2C).

As lipid peroxidation is a central hallmark of ferroptosis and is typically accompanied by increased ROS levels, we assessed ROS content in tumor tissues. ROS levels in the combination group were markedly higher than in the model ($p < 0.001$) and monotherapy groups ($p < 0.05$), confirming that the combination therapy induces lipid peroxide accumulation to trigger ferroptosis (Fig. 2D). Western blotting revealed that, compared with the model group, the combination therapy markedly upregulated the ferroptosis-promoting protein ACSL4 ($p < 0.001$) and significantly downregulated ferroptosis-suppressing proteins GPX4, DMT1, HSBP1, and SLC7A11 ($p < 0.001$, Fig. 2E), as evidenced by qRT-PCR at the mRNA level ($p < 0.001$, Fig. 2F). Collectively, these molecular alterations are consistent with the ferroptotic phenotype, strongly supporting the involvement of ferroptosis in the antitumor effect of the combination therapy.

Combination Therapy Markedly Upregulates STEAP4 Expression in Tumor Tissues

To explore potential molecular targets underlying the synergistic effect, transcriptome sequencing was performed on paired gastric cancer and adjacent non-tumor tissues. Intersection analysis between DEGs (differentially expressed genes) and ferroptosis-related genes from public databases identified 21 overlapping candidates, which were visualized in volcano and Venn plots (Fig. 3A,B). Subsequent functional annotation using KEGG and GO enrichment analyses confirmed that these genes were enriched in ferroptosis-related pathways (Fig. 3C,D), and their expression profiles were presented in a heatmap (Fig. 3E).

Given the established role of *STEAP4* in iron metabolism, we examined its protein expression in tumor tissues. *STEAP4* protein expression was moderately increased in the two monotherapy groups compared with the model group, but yielded the highest level in the combination group compared to all other groups ($p < 0.05$, Fig. 3F). qRT-PCR analysis confirmed these observations at the transcriptional level ($p < 0.05$, Fig. 3G). These findings suggest that *STEAP4* upregulation may represent a key molecular event mediating the synergistic antitumor effect of oxaliplatin combined with PD-1 inhibition.

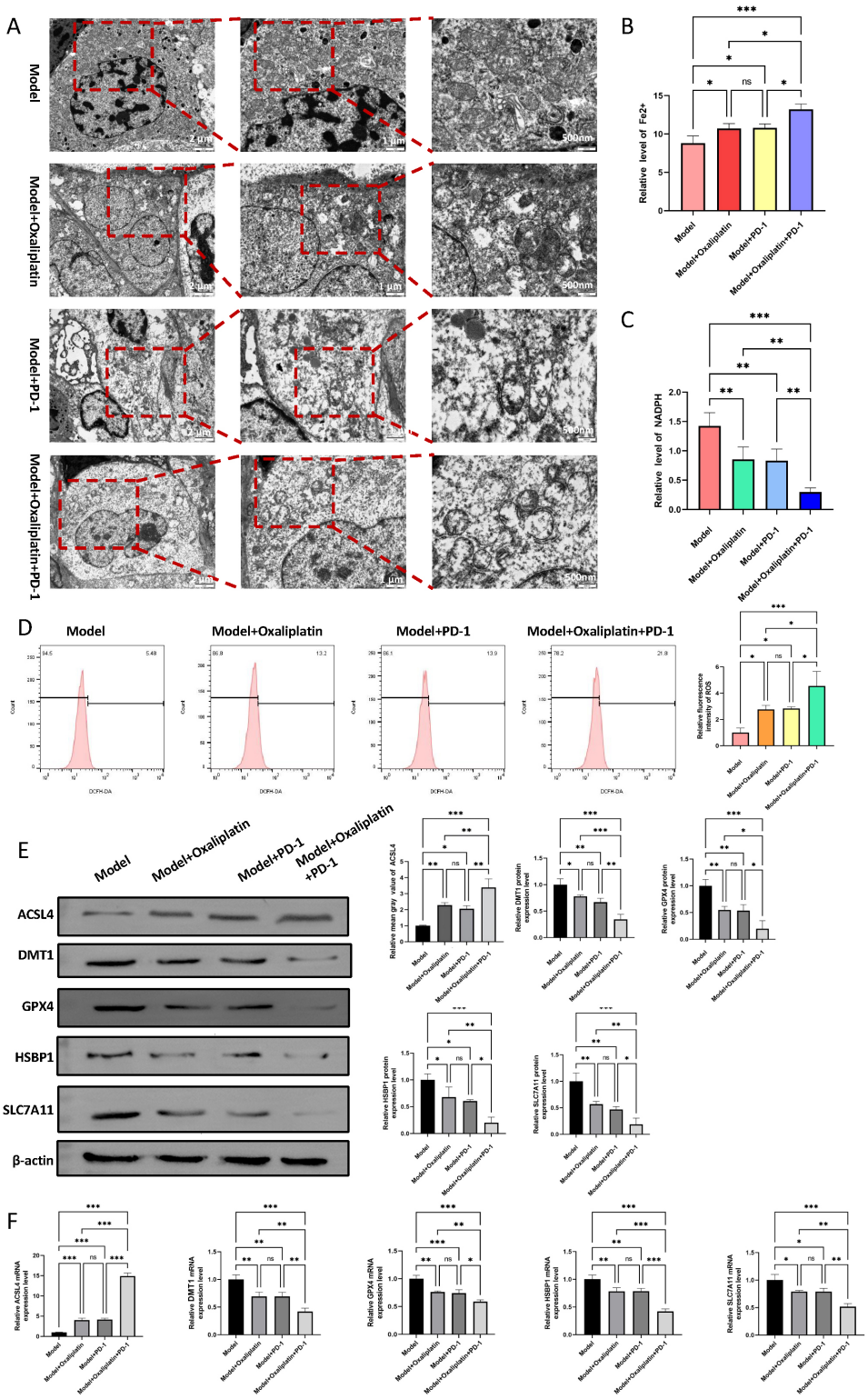

Fig. 2. Oxaliplatin combined with a PD-1 inhibitor exerts antitumor effects by inducing ferroptosis. (A) Transmission electron microscopy images showing ultrastructural features of mitochondria in tumor tissues specimens (from left to right, scale bar = 2 µm, 1 µm, 500 nm, respectively). (B) Measurement of ferrous ion (Fe^{2+}) concentrations in tumor tissues. (C) Measurement of NADPH levels in tumor tissues. (D) Measurement of reactive oxygen species (ROS) levels in tumor tissues. (E) Western blot analysis of ferroptosis-related proteins (ACSL4, DMT1, GPX4, HSBP1, and SLC7A11) in tumor tissues. (F) qRT-PCR analysis of ferroptosis-related (*ACSL4*, *DMT1*, *GPX4*, *HSBP1*, and *SLC7A11*) mRNA expression in tumor tissues. Data are presented as mean ± SD from three biologically independent experiments. ns: not significant, *$p < 0.05$, **$p < 0.01$, ***$p < 0.001$.

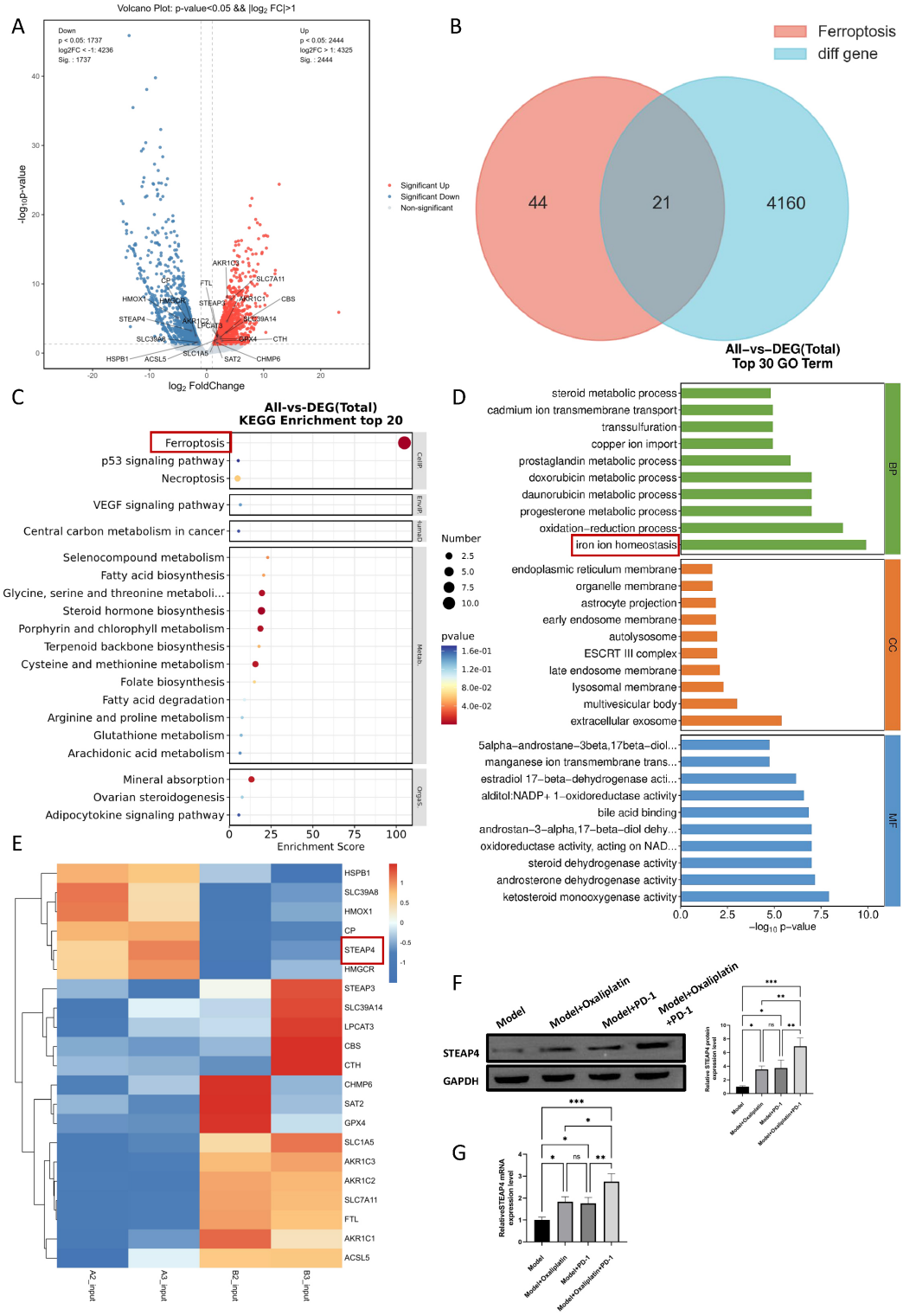

Fig. 3. Oxaliplatin combined with a PD-1 inhibitor upregulates STEAP4 expression in tumor tissues. (A) Volcano plot of differentially expressed genes (DEGs) between gastric cancer and adjacent tissues. (B) Venn diagram showing the intersection of DEGs and ferroptosis-related genes. (C,D) KEGG and GO enrichment analyses of the intersecting genes. The red box in (C) showed that these genes were enriched in ferroptosis-related pathways through KEGG enrichment analyses; The red box in (D) showed that these genes were enriched in ferroptosis-related pathways through GO enrichment analyses. (E) Heatmap of intersecting gene expression. The red box in (E) showed that *STEAP4* was enriched in ferroptosis-related pathways. (F) Western blot analysis of *STEAP4* protein expression in tumor tissues from each treatment group. (G) qRT-PCR analysis of *STEAP4* mRNA expression. Data are presented as mean ± SD from three biologically independent experiments. ns: not significant, *$p < 0.05$, **$p < 0.01$, ***$p < 0.001$.

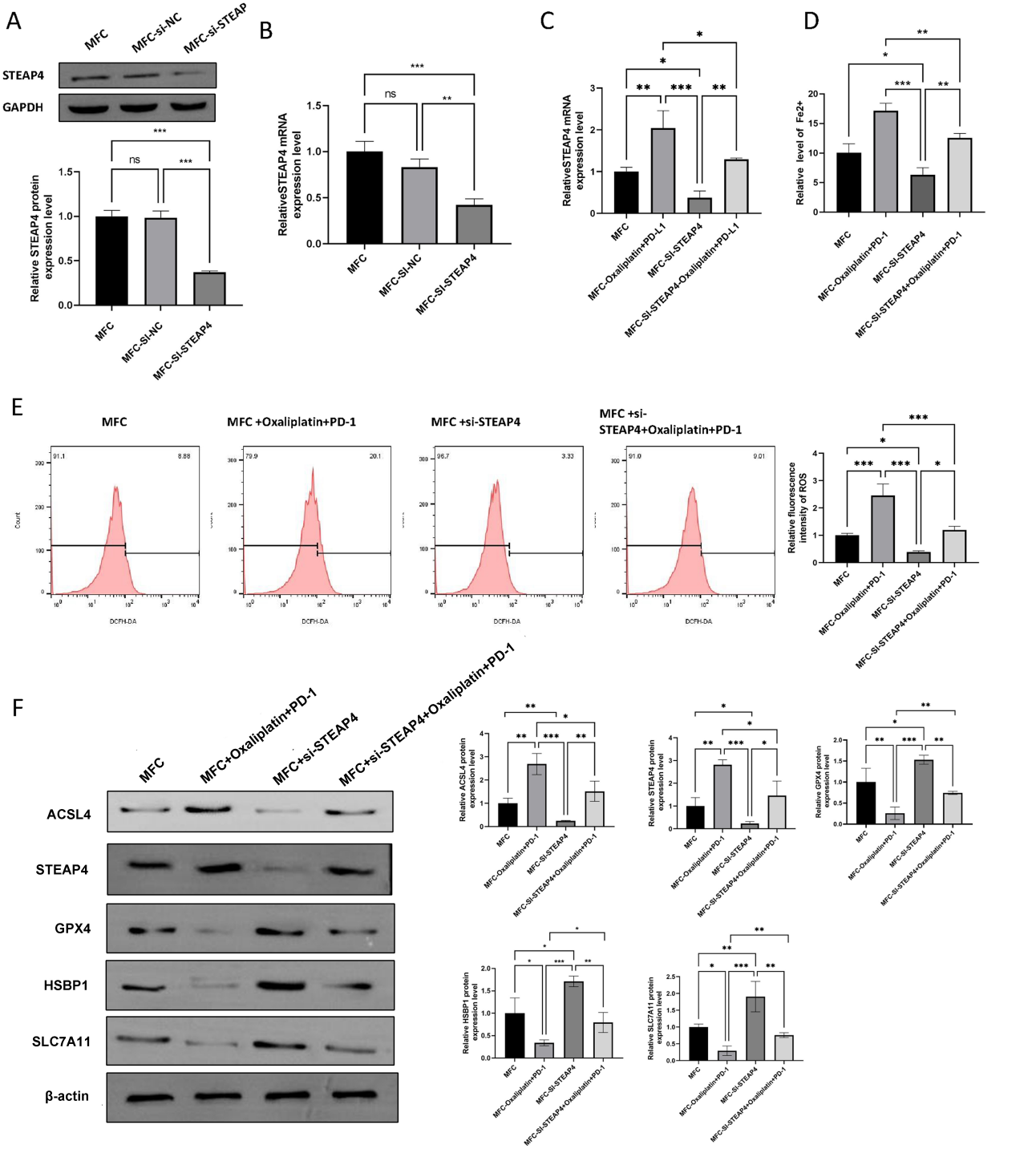

Fig. 4. STEAP4 knockdown reduces cell sensitivity to combination therapy and suppresses ferroptosis. (A,B) Western blot and qRT-PCR validation of *STEAP4* knockdown efficiency in MFC cells via siRNA and plasmid transfection. (C) qRT-PCR analysis of *STEAP4* mRNA expression in MFC cells under different treatment conditions. (D) Measurement of intracellular ferrous ion (Fe^{2+}) concentrations in MFC cells following combination therapy with or without *STEAP4* knockdown. (E) Measurement of intracellular ROS levels in MFC cells following combination therapy with or without *STEAP4* knockdown. (F) Western blot analysis of key regulators involved in ferroptosis-related proteins (ACSL4, STEAP4, GPX4, HSBP1, and SLC7A11) in MFC cells following combination therapy with or without *STEAP4* knockdown. Data are presented as mean ± SD from three biologically independent experiments. ns: not significant, *$p < 0.05$, **$p < 0.01$, ***$p < 0.001$.

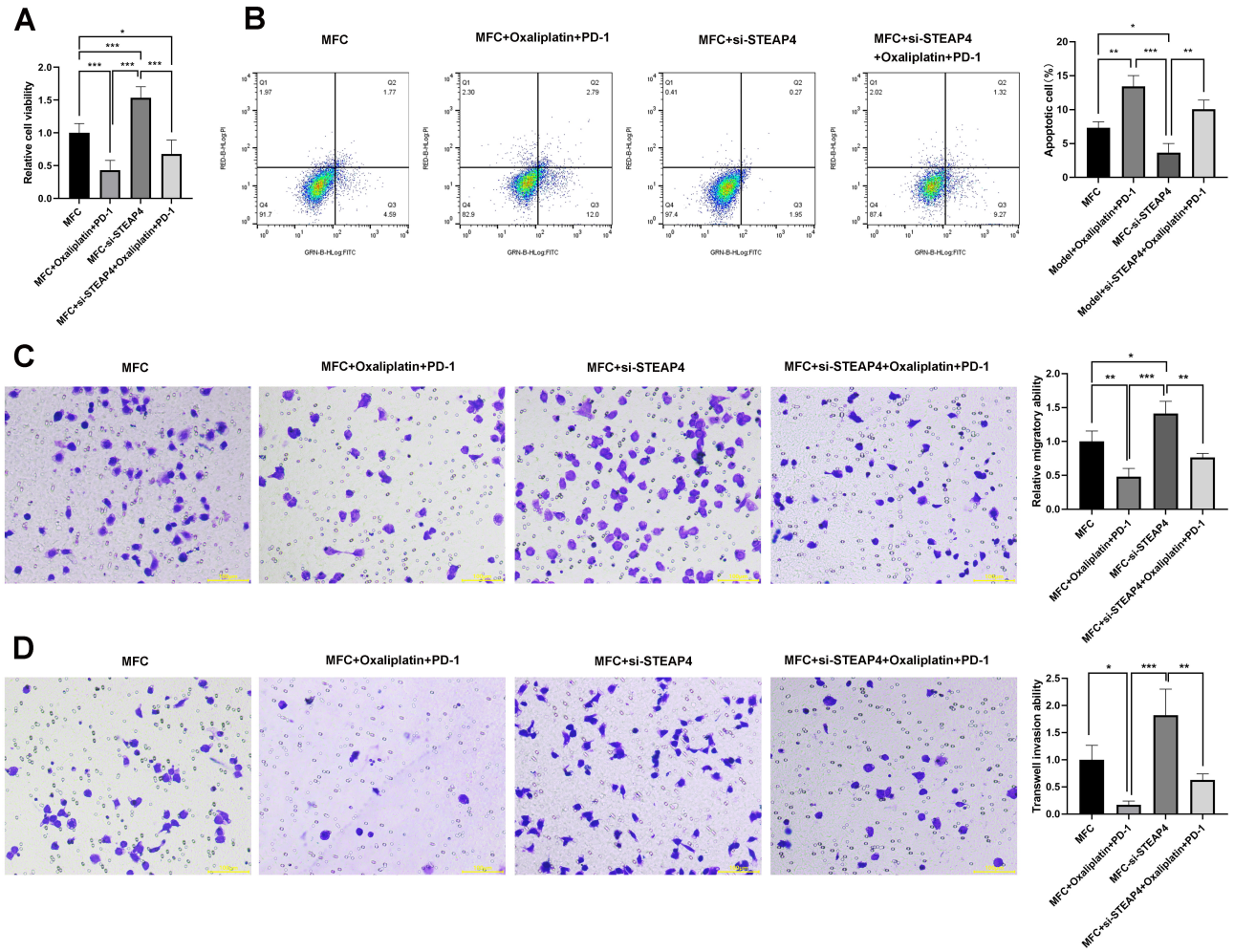

Fig. 5. STEAP4 knockdown reduces cell viability, migration, invasion to combination therapy and suppresses cell apoptosis. (A) CCK8 analysis of cell viability of MFC cells. Data are presented as mean ± SD relative to the control group (MFC, set as 1.0). (B) The cell apoptosis in MFC cells following combination therapy with or without *STEAP4* knockdown was tested through flow cytometry. (C) The cell migration was measured through Transwell assay in MFC cells following combination therapy with or without *STEAP4* knockdown. (D) The cell invasion was measured through Transwell assay in MFC cells following combination therapy with or without *STEAP4* knockdown. Data are presented as mean ± SD. *$p < 0.05$, **$p < 0.01$, ***$p < 0.001$.

STEAP4 Knockdown Reduces Cell Sensitivity to Oxaliplatin Plus PD-1 Inhibitor In Vitro

To directly assess the functional role of *STEAP4* in the combination therapy, *STEAP4* knockdown experiments were conducted in MFC cells. Western blot and qRT-PCR analyses confirmed efficient suppression of *STEAP4* expression in si-*STEAP4*–transfected cells compared with si-NC controls ($p < 0.001$, $p < 0.01$, Fig. 4A,B). We next evaluated the effect of *STEAP4* knockdown on treatment efficacy. qRT-PCR analysis of MFC cells from different treatment groups (MFC, MFC + oxaliplatin + PD-1 inhibitor, MFC + si-*STEAP4*, MFC + oxaliplatin + PD-1 inhibitor + si-*STEAP4*) showed that combination therapy increased *STEAP4* mRNA expression ($p < 0.01$). After *STEAP4* knockdown, the high expression of *STEAP4* caused by the combined treatment decreased ($p < 0.05$, Fig. 4C). Mechanistically, *STEAP4* knockdown reversed the ferroptotic phenotype induced by the combination therapy, as evidenced by significant reductions in intracellular Fe^{2+} and ROS levels compared with the combination group ($p < 0.01$, $p < 0.001$, Fig. 4D,E). Western blot analysis further demonstrated that *STEAP4* knockdown suppressed ACSL4 expression while restoring GPX4 and SLC7A11 expression in the context of combination therapy ($p < 0.05$, $p < 0.01$, Fig. 4F). Notably, HSBP1 exhibited a divergent expression pattern: it was elevated by single-agent treatments yet reduced by the combination therapy, although these alterations were not statistically significant. This suggests that HSBP1 may be regulated through a mechanism distinct from the STEAP4-mediated ferroptosis pathway.

Cellular functional assays also further revealed the functional impact of *STEAP4* knockdown on cellular phenotype. CCK8 assays demonstrated that *STEAP4* knockdown significantly attenuated the reduction in cell viabil-

ity induced by combination therapy ($p < 0.001$, Fig. 5A). Flow cytometry analysis showed that apoptosis levels were markedly decreased in cells with si-*STEAP4* compared to those receiving combination therapy ($p < 0.001$, Fig. 5B). Additionally, Transwell assays indicated that *STEAP4* knockdown restored both migratory and invasive capacities of MFC cells that were otherwise suppressed by the combination treatment ($p < 0.01$, $p < 0.001$, Fig. 5C,D). These findings strongly indicate that *STEAP4* upregulation is essential for inducing ferroptosis and achieving the synergistic antitumor effect of the combination therapy, whereas its downregulation impairs therapeutic efficacy.

Discussion

The treatment of gastric cancer has entered an era of multimodal strategies, including chemotherapy, targeted therapy, and immunotherapy. Optimizing combination regimens to maximize therapeutic efficacy remains a central challenge in both clinical and translational research [22]. Although the synergistic effect of oxaliplatin combined with PD-1 inhibitors in gastric cancer has been widely reported, existing studies have mostly focused on the remodeling of the immune microenvironment [23,24], while ignoring the impact of ferroptosis, an emerging form of cell death, on treatment sensitivity. This study systematically demonstrated the synergistic effect of oxaliplatin combined with a PD-1 inhibitor in gastric cancer, and, innovatively, revealed that this synergy is mediated through the *STEAP4*-dependent ferroptosis pathway.

Our *in vivo* results confirmed the synergistic antitumor activity of oxaliplatin and PD-1 blockade, consistent with the current clinical trend toward chemo-immunotherapy. Oxaliplatin directly kills tumor cells via DNA damage, and may also enhance antitumor immunity by releasing neoantigens, upregulating MHC class I expression, and promoting dendritic cell maturation, key steps in converting "cold" tumors into "hot" [25–27]. This immunogenic shift enables PD-1 inhibitors to unleash activated T cells, allowing them to efficiently recognize and eradicate chemotherapy-"tagged" tumor cells [28–30]. Our findings provide robust experimental evidence in support of this theoretical framework.

The most significant discovery of this study is the identification of *STEAP4* as a key mediator of this synergy. *STEAP4*, a metalloreductase localized to the plasma membrane and endosomes, catalyzes the reduction of Fe^{3+} to Fe^{2+}—a critical step in cellular iron metabolism [20, 31,32]. We observed that combination therapy markedly upregulated *STEAP4* expression, whereas *STEAP4* knockdown *in vitro* attenuated the therapeutic benefit. These results suggest that *STEAP4* may function as a sensitizing factor in gastric cancer therapy.

Mechanistically, *STEAP4* links directly to ferroptosis, a form of regulated cell death driven by Fe^{2+}-catalyzed Fenton reactions that generate abundant lipid ROS, ultimately causing membrane damage [33–35]. *STEAP4* upregulation may promote ferroptosis via: (1) disrupting intracellular iron homeostasis, leading to transient or localized Fe^{2+} overload; and (2) perturbing the redox balance, thereby impairing the cell's antioxidant defenses. Our Western blot analysis strongly supports this hypothesis. GPX4, a pivotal ferroptosis defense protein, requires glutathione (GSH) for activity, and GSH synthesis depends on cystine uptake mediated by SLC7A11 (part of the xCT system) [36–38]. Combination therapy downregulated GPX4 and SLC7A11, while upregulating ACSL4—a pro-ferroptotic enzyme that esterifies long-chain polyunsaturated fatty acids, providing substrates for lipid peroxidation. *STEAP4* knockdown reverses these changes, suppressing ACSL4 while restoring GPX4 and SLC7A11, thereby diminishing ferroptosis induction. Functionally, ACSL4 upregulation acts as "fuel" for ferroptosis, and the coordinated shifts in these protein levels converge on ferroptotic cell death as a central mechanism.

This study for the first time reveals the key role of *STEAP4* in the treatment of gastric cancer with oxaliplatin combined with PD-1 inhibitors, enhancing treatment sensitivity by promoting ferroptosis. These findings carry important translational relevance in two key aspects. First, *STEAP4* expression may serve as a predictive biomarker for stratifying patients with gastric cancer likely to respond to oxaliplatin plus PD-1 inhibitor therapy. High *STEAP4* expression may appear to sensitize tumours to this regimen. Second, *STEAP4* itself represents a potential therapeutic target; pharmacological strategies that enhance *STEAP4* its expression, when combined with chemo-immunotherapy, could further improve clinical outcomes.

Nevertheless, this study has limitations. First, the use of a single gastric cancer cell line and its corresponding nude mouse xenograft model influences the generalizability of our conclusions; therefore, validation across additional molecular subtypes, patient-derived xenograft (PDX) models, and clinical specimens is required. Second, although *STEAP4* silencing *STEAP4* partially attenuated ferroptosis and drug sensitivity, an *in vivo* rescue effect of ferroptosis inhibitors (e.g., Ferrostatin-1 or liproxstatin-1) was not examined. Future studies incorporating a 'combination therapy + ferroptosis inhibitor' regimen are needed to rigorously test whether ferroptosis is an essential mechanism underlying the observed synergy in GC treatment. Furthermore, the upstream regulatory mechanisms by which the combination therapy modulates *STEAP4* transcription or translation remain unclear and warrant further investigation.

Conclusion

In summary, our study demonstrates a potent synergistic antitumor effect of oxaliplatin and PD-1 blockade

in gastric cancer. This synergy is closely associated with the upregulation of *STEAP4*, which promotes ferroptosis and enhances tumor sensitivity to the combination therapy. These findings provide a new mechanistic basis for chemoimmunotherapy in gastric cancer and identify *STEAP4* as a dual-functional candidate—serving as both a promising predictive biomarker and a potential therapeutic target for this strategy.

Availability of Data and Materials

The datasets used and/or analyzed during the current study are available from the corresponding author via email request.

Author Contributions

All authors have made substantial contributions to the work and meet all four ICMJE authorship criteria. Specifically: XQJ conceived and designed the study. YXZ, LF and FXD were responsible for the acquisition, analysis, and interpretation of data. FXD and LF contributed to the literature review and drafted the initial manuscript. XQJ and YXZ critically revised the manuscript for important intellectual content. All authors reviewed and approved the final version to be published, and agree to be accountable for all aspects of the work, ensuring that questions related to the accuracy or integrity of any part of the work are appropriately investigated and resolved.

Ethics Approval and Consent to Participate

All animal experiments were approved by the Institutional Animal Care and Use Committee of Yi Shengyuan Gene Technology (Tianjin) Co., Ltd. (protocol number YSY-DWLL-2023809).

Acknowledgment

Not applicable.

Funding

This work was supported by the Natural Science Foundation of Inner Mongolia Autonomous Region (2024LHMS08013); the Scientific Research Joint Fund of Public Hospitals (2024GLLH0397); the Demonstration Project for the Transformation and High-quality Development of Public Hospitals (2024YNQN002).

Conflict of Interest

The authors declare no conflict of interest.

References

[1] Tan N, Wu H, Cao M, Yang F, Yan X, He S, *et al*. Global, regional, and national burden of early-onset gastric cancer. Cancer Biology & Medicine. 2024; 21: 667–678. https://doi.org/10.20892/j.issn.2095-3941.2024.0159.

[2] Yang L, Ying X, Liu S, Lyu G, Xu Z, Zhang X, *et al*. Gastric cancer: Epidemiology, risk factors and prevention strategies. Chinese Journal of Cancer Research. 2020; 32: 695–704. https://doi.org/10.21147/j.issn.1000-9604.2020.06.03.

[3] Renzulli M, Clemente A, Spinelli D, Ierardi AM, Marasco G, Farina D, *et al*. Gastric Cancer Staging: Is It Time for Magnetic Resonance Imaging? Cancers. 2020; 12: 1402. https://doi.org/10.3390/cancers12061402.

[4] Luo HY, Xu RH, Zhang L, Li YH, Shi YX, Lin TY, *et al*. A pilot study of oxaliplatin, fluorouracil and folinic acid (FOLFOX-6) as first-line chemotherapy in advanced or recurrent gastric cancer. Chemotherapy. 2008; 54: 228–235. https://doi.org/10.1159/000140467.

[5] Garrido M, Melgoza G, Galindo H, Madrid J, Sánchez C, Nervi B, *et al*. Treatment of advanced gastric cancer with oxaliplatin plus 5-fluorouracil/ leucovorin (FOLFOX-4 chemotherapy). Revista Medica De Chile. 2007; 135: 1380–1387. http://doi.org/10.4067/S0034-98872007001100003. (In Spanish)

[6] Xu Z, Liang J, Fu R, Yang L, Xin Chen Y, Ren W, *et al*. Effect of PD-L1 Expression for the PD-1/L1 Inhibitors on Non-small Cell Lung Cancer: A Meta-analysis Based on Randomised Controlled Trials. Clinical Oncology. 2023; 35: 640–651. https://doi.org/10.1016/j.clon.2023.07.012.

[7] Li Y, Liang X, Li H, Chen X. Efficacy and safety of immune checkpoint inhibitors for advanced non-small cell lung cancer with or without PD-L1 selection: A systematic review and network meta-analysis. Chinese Medical Journal. 2023; 136: 2156–2165. https://doi.org/10.1097/CM9.0000000000002750.

[8] Balança CC, Scarlata CM, Michelas M, Devaud C, Sarradin V, Franchet C, *et al*. Dual Relief of T-lymphocyte Proliferation and Effector Function Underlies Response to PD-1 Blockade in Epithelial Malignancies. Cancer Immunology Research. 2020; 8: 869–882. https://doi.org/10.1158/2326-6066.CIR-19-0855.

[9] Cai MC, Zhao X, Cao M, Ma P, Chen M, Wu J, *et al*. T-cell exhaustion interrelates with immune cytolytic activity to shape the inflamed tumor microenvironment. The Journal of Pathology. 2020; 251: 147–159. https://doi.org/10.1002/path.5435.

[10] Muro K, Chung HC, Shankaran V, Geva R, Catenacci D, Gupta S, *et al*. Pembrolizumab for patients with PD-L1-positive advanced gastric cancer (KEYNOTE-012): a multicentre, open-label, phase 1b trial. The Lancet. Oncology. 2016; 17: 717–726. https://doi.org/10.1016/S1470-2045(16)00175-3.

[11] Fuchs CS, Doi T, Jang RW, Muro K, Satoh T, Machado M, *et al*. Safety and Efficacy of Pembrolizumab Monotherapy in Patients With Previously Treated Advanced Gastric and Gastroesophageal Junction Cancer: Phase 2 Clinical KEYNOTE-059 Trial. JAMA Oncology. 2018; 4: e180013. https://doi.org/10.1001/jamaoncol.2018.0013.

[12] Krysko DV, Garg AD, Kaczmarek A, Krysko O, Agostinis P, Vandenabeele P. Immunogenic cell death and DAMPs in cancer therapy. Nature Reviews. Cancer. 2012; 12: 860–875. https://doi.org/10.1038/nrc3380.

[13] Galluzzi L, Humeau J, Buqué A, Zitvogel L, Kroemer G. Immunostimulation with chemotherapy in the era of immune checkpoint inhibitors. Nature Reviews. Clinical Oncology. 2020; 17: 725–741. https://doi.org/10.1038/s41571-020-0413-z.

[14] Opzoomer JW, Sosnowska D, Anstee JE, Spicer JF, Arnold JN. Cytotoxic Chemotherapy as an Immune Stimulus: A Molecular Perspective on Turning Up the Immunological Heat on Can-

cer. Frontiers in Immunology. 2019; 10: 1654. https://doi.org/10.3389/fimmu.2019.01654.

[15] Zhang M, Guo M, Gao Y, Wu C, Pan X, Huang Z. Mechanisms and therapeutic targets of ferroptosis: Implications for nanomedicine design. Journal of Pharmaceutical Analysis. 2024; 14: 100960. https://doi.org/10.1016/j.jpha.2024.03.001.

[16] Kong Y, Li J, Lin R, Lu S, Rong L, Xue Y, *et al*. Understanding the unique mechanism of ferroptosis: a promising therapeutic target. Frontiers in Cell and Developmental Biology. 2024; 11: 1329147. https://doi.org/10.3389/fcell.2023.1329147.

[17] Wang W, Green M, Choi JE, Gijón M, Kennedy PD, Johnson JK, *et al*. CD8$^+$ T cells regulate tumour ferroptosis during cancer immunotherapy. Nature. 2019; 569: 270–274. https://doi.org/10.1038/s41586-019-1170-y.

[18] Zhou X, Li Y, Zhang X, Li B, Jin S, Wu M, *et al*. Hemin blocks TIGIT/PVR interaction and induces ferroptosis to elicit synergistic effects of cancer immunotherapy. Science China. Life Sciences. 2024; 67: 996–1009. https://doi.org/10.1007/s11427-023-2472-4.

[19] Cai Q, Jing C, Wang X, Xing X, Liu W. STEAP Proteins: Roles in disease biology and potential for therapeutic intervention. International Journal of Biological Macromolecules. 2025; 309: 142797. https://doi.org/10.1016/j.ijbiomac.2025.142797.

[20] Scarl RT, Lawrence CM, Gordon HM, Nunemaker CS. STEAP4: its emerging role in metabolism and homeostasis of cellular iron and copper. The Journal of Endocrinology. 2017; 234: R123–R134. https://doi.org/10.1530/JOE-16-0594.

[21] Fan S, Xia Z, Liu W, Zhu Y, Liu X, Gu P, *et al*. STEAP4 facilitates growth, migration, and invasion of prostate carcinoma through upregulation of NOTCH4. FASEB Journal. 2025; 39: e70508. https://doi.org/10.1096/fj.202403129RR.

[22] Roviello G, Rodriquenz MG, Aprile G, D'Angelo A, Roviello F, Nobili S, *et al*. Maintenance in gastric cancer: New life for an old issue? Critical Reviews in Oncology/Hematology. 2021; 160: 103307. https://doi.org/10.1016/j.critrevonc.2021.103307.

[23] Xu C, Xie X, Kang N, Jiang H. Neoadjuvant PD-1 inhibitor and apatinib combined with S-1 plus oxaliplatin for locally advanced gastric cancer patients: a multicentered, prospective, cohort study. Journal of Cancer Research and Clinical Oncology. 2023; 149: 4091–4099. https://doi.org/10.1007/s00432-022-04302-9.

[24] Tang Y, Dai L, Wang Z, Zhang M, Xie H, Yang Y, *et al*. Short term efficacy and safety of PD-1 inhibitor and apatinib plus S-1 and oxaliplatin as neoadjuvant chemotherapy for patients with locally advanced gastric cancer. Medicine. 2024; 103: e40572. https://doi.org/10.1097/MD.0000000000040572.

[25] Tang L, Cai D, Qin M, Lu S, Hu MH, Ruan S, *et al*. Oxaliplatin-Based Platinum(IV) Prodrug Bearing Toll-like Receptor 7 Agonist for Enhanced Immunochemotherapy. ACS Omega. 2019; 5: 726–734. https://doi.org/10.1021/acsomega.9b03381.

[26] Wang X, Li M, Ren K, Xia C, Li J, Yu Q, *et al*. On-Demand Autophagy Cascade Amplification Nanoparticles Precisely Enhanced Oxaliplatin-Induced Cancer Immunotherapy. Advanced Materials. 2020; 32: e2002160. https://doi.org/10.1002/adma.202002160.

[27] Zhu H, Shan Y, Ge K, Lu J, Kong W, Jia C. Oxaliplatin induces immunogenic cell death in hepatocellular carcinoma cells and synergizes with immune checkpoint blockade therapy. Cellular Oncology. 2020; 43: 1203–1214. https://doi.org/10.1007/s13402-020-00552-2.

[28] Ludin A, Zon LI. Cancer immunotherapy: The dark side of PD-1 receptor inhibition. Nature. 2017; 552: 41–42. https://doi.org/10.1038/nature24759.

[29] Romano E, Romero P. The therapeutic promise of disrupting the PD-1/PD-L1 immune checkpoint in cancer: unleashing the CD8 T cell mediated anti-tumor activity results in significant, unprecedented clinical efficacy in various solid tumors. Journal for Immunotherapy of Cancer. 2015; 3: 15. https://doi.org/10.1186/s40425-015-0059-z.

[30] Chen J, Sun HW, Yang YY, Chen HT, Yu XJ, Wu WC, *et al*. Reprogramming immunosuppressive myeloid cells by activated T cells promotes the response to anti-PD-1 therapy in colorectal cancer. Signal Transduction and Targeted Therapy. 2021; 6: 4. https://doi.org/10.1038/s41392-020-00377-3.

[31] Oosterheert W, van Bezouwen LS, Rodenburg RNP, Granneman J, Förster F, Mattevi A, *et al*. Cryo-EM structures of human STEAP4 reveal mechanism of iron(III) reduction. Nature Communications. 2018; 9: 4337. https://doi.org/10.1038/s41467-018-06817-7.

[32] Zhou J, Ye S, Fujiwara T, Manolagas SC, Zhao H. Steap4 plays a critical role in osteoclastogenesis in vitro by regulating cellular iron/reactive oxygen species (ROS) levels and cAMP response element-binding protein (CREB) activation. The Journal of Biological Chemistry. 2013; 288: 30064–30074. https://doi.org/10.1074/jbc.M113.478750.

[33] Wang Y, Li C, Zhuo J, Hui H, Zhou B, Tian J. The Detection of Divalent Iron and Reactive Oxygen Species During Ferroptosis with the Use of a Dual-Reaction Turn-On Fluorescent Probe. Molecular Imaging and Biology. 2023; 25: 423–434. https://doi.org/10.1007/s11307-022-01774-6.

[34] Dixon SJ, Stockwell BR. The role of iron and reactive oxygen species in cell death. Nature Chemical Biology. 2014; 10: 9–17. https://doi.org/10.1038/nchembio.1416.

[35] Qian W, Zhang C, He L, Jin S, Suo R, Li Y, *et al*. X-ray induced in-situ ferroptosis through the Fenton reaction of iron supplements for the cancer therapy. Bioorganic Chemistry. 2025; 154: 108021. https://doi.org/10.1016/j.bioorg.2024.108021.

[36] Yang WS, SriRamaratnam R, Welsch ME, Shimada K, Skouta R, Viswanathan VS, *et al*. Regulation of ferroptotic cancer cell death by GPX4. Cell. 2014; 156: 317–331. https://doi.org/10.1016/j.cell.2013.12.010.

[37] Lee N, Carlisle AE, Peppers A, Park SJ, Doshi MB, Spears ME, *et al*. xCT-Driven Expression of GPX4 Determines Sensitivity of Breast Cancer Cells to Ferroptosis Inducers. Antioxidants. 2021; 10: 317. https://doi.org/10.3390/antiox10020317.

[38] Forcina GC, Dixon SJ. GPX4 at the Crossroads of Lipid Homeostasis and Ferroptosis. Proteomics. 2019; 19: e1800311. https://doi.org/10.1002/pmic.201800311.